Lawrence Berkeley National Laboratory

Title

A reduced-order model of concentration polarization in reverse osmosis systems with feed spacers

Permalink

https://escholarship.org/uc/item/6gx5w0vk

Authors

Johnston, Jacob
Dischinger, Sarah M
Nassr, Mostafa
et al.

Publication Date

2023-06-01

DOI

10.1016/j.memsci.2023.121508

Copyright Information

Peer reviewed

A reduced-order model of concentration polarization in reverse osmosis systems with feed spacers

Jacob Johnston [a], Sarah M. Dischinger [b], Mostafa Nassr [d], Ji Yeon Lee [e], Pedram Bigdelou [a], Benny D. Freeman [d], Kristofer L. Gleason [d], Denis Martinand [c], Daniel J. Miller [b], Sergi Molins [f], Nicolas Spycher [f], William T. Stringfellow [e], Nils Tilton [a],*

[a] *Mechanical Engineering, Colorado School of Mines, Golden CO, USA*
[b] *Chemical Sciences Division, Lawrence Berkeley National Laboratory, Berkeley CA, USA*
[c] *Aix-Marseille University, CNRS, Centrale Marseille, M2P2, , Marseille, France*
[d] *John J. McKetta Jr. Department of Chemical Engineering, The University of Texas at Austin, Austin, TX, USA*
[e] *Energy Geosciences Division, Lawrence Berkeley National Laboratory, Berkeley CA, USA*
[f] *Earth & Environmental Sciences Area, Lawrence Berkeley National Laboratory, Berkeley CA, USA*

ARTICLE INFO

ABSTRACT

Feed spacers in reverse osmosis systems generate complex fluid flows that limit computational fluid dynamics (CFD) simulations to small length and time scales. That limits our ability to simulate mineral scaling and other membrane fouling phenomena, which occur over longer length and time scales. Thus motivated, we develop a reduced model that replaces the CFD simulation of the velocity field with an analytical model that mimics spacers. This focuses the remaining numerical effort on simulating the advection–diffusion equation governing solute transport. We motivate and validate the model with CFD simulations and bench-scale experiments of spacer filaments in three different arrangements, including cases of unsteady vortex shedding. We show that the model produces a roughly 10,000-fold speedup compared to CFD, and accurately reproduces CFD predictions of not only the average and maximum concentrations, but also the local concentration distribution along the membrane. We also demonstrate the model for simulating a feed channel with a length-to-height ratio of 200. The model provides a simple testbed for exploratory studies of multispecies transport, precipitation, and membrane fouling phenomena for which simulating spacers is often prohibitive.

1. Introduction

This study is motivated by the recent development of high-recovery reverse osmosis (RO) systems that concentrate brines far further than conventional RO. Examples include closed-circuit [1–4], osmotically-assisted [5], low-salt-rejection [6], and high-pressure [7] RO. These systems all face the challenges of concentration polarization and mineral scaling. Polarization is the accumulation of solutes adjacent to the membrane. This leads to scaling, the precipitation of salts onto the membrane, which blocks pores and damages the membrane. Scaling is governed by a complicated combination of hydrodynamics, multi-species transport, and the chemical kinetics and thermodynamics of crystal nucleation and growth [8–14]. Simulating these coupled processes numerically is made all the more challenging by the presence of feed spacers, a plastic mesh that separates tightly-packed membrane sheets in RO systems [15]. Though reactive transport models now exist that can simulate precipitation reactions [16], such codes typically

cannot simulate the Navier–Stokes equations in feed channels with spacers. Simply adding that ability will not solve the issue, because current methods of computational fluid dynamics (CFD) cannot simulate spacers over the length and time-scales relevant to mineral scaling. Thus motivated, our objective is to explore low-computational-cost reduced models of feed spacers that could allow reactive transport codes to simulate mineral scaling. Such codes could then inform the design and operation of high-recovery RO systems.

Spacers generate two major challenges to simulating mineral scaling with CFD. The first is a disparity in length scales. RO modules have feed channels roughly one meter long, while spacers are composed of plastic filaments with diameters less than one millimeter [15]. These filaments generate equally small vortical flow structures that play a critical role in concentration polarization [17,18]. Simulating these structures over the length of an RO module is currently not feasible, except with large supercomputers, and even then, only under idealized

---

* Corresponding author.
E-mail address: ntilton@mines.edu (N. Tilton).

Nomenclature

α	osmotic pressure constant (Pa l/ g)
β	offset used in Eq. (28) (unitless)
C_{in}	inlet concentration (g/l)
δ	boundary layer depth (m)
$\gamma(x)$	gradient in Eq. (24)
$\hat{y}$	shifted coordinate in Eq. (25) (m)
λ	wavelength (see Eq. (15)) (m)
μ	dynamic viscosity (Pa s)
$\mathcal{K}$	membrane permeance (LMH/bar)
Π	osmotic pressure $\Pi = \alpha c_m$ (Pa)
P_{out}	outlet pressure (Pa)
ρ	density (kg/m^3)
U_{in}	mean inlet velocity (m/s)
$\widetilde{u}$	shape function in Eq. (15) (m/s)
$\mathbf{v}$	velocity vector (m/s)
$\mathbf{v}_b$	base flow (see Eq. (9)) (m/s)
$\mathbf{v}_p$	perturbation flow (see Eq. (9)) (m/s)
$\widetilde{v}$	shape function in Eq. (15) (m/s)
A	vortex amplitude (unitless)
a_0, a_1, a_2	coefficients in Eq. (25) (unitless)
A_{max}	vortex strength at which C_{max}^* occurs (unitless)
b	model parameter controlling vortex height, d (see Eq. (19)) (unitless)
c	salt concentration (g/l)
C_{max}^*	maximum salt concentration for fixed b and Re (g/l)
$c_m(x)$	salt concentration at membrane surface(g/l)
C_{max}	maximum concentration in window-of-interest (g/l)
C_{max}^{CFD}	CFD prediction for maximum concentration (see Eq. (22)) (g/l)
C_{max}^{mod}	model prediction for maximum concentration (see Eq. (22)) (g/l)
C_{osm}	effective average concentration (g/l)
d	vortex height (see Eq. (20)) (m)
E	weighted error for model fitting (see Eq. (21)) (unitless)
E_C	weighted error for concentration in model fitting (see Eq. (22)) (unitless)
E_J	weighted error for flux in model fitting (see Eq. (22)) (unitless)
$f(y)$	parabolic profile in Eq. (10) (unitless)
G	wave amplitude in Eq. (28) (unitless)
h	channel height (m)
J	permeate flux produced in window-of-interest (LMH)
J^0	permeate flux produced by base flow (LMH)
J^{CFD}	CFD prediction for flux (see Eq. (22)) (LMH)
J^{mod}	model prediction for flux (see Eq. (22)) (LMH)
L	channel length (m)
L_{out}	appended outlet length (m)
p	pressure (Pa)
Re	Reynolds number $Re = \rho U_{in} h/\mu$ (unitless)
Re_c	critical Reynolds number (unitless)
t	time (s)
u, v	velocity components along x and y directions (m/s)
$U(x)$	local mean feed velocity in base flow (see Eq. (10)) (m/s)
u^*	CFD result for $u - U_{in}$ (see Eq. (23)) (m/s)
$v_m(x)$	permeate velocity (m/s)
x, y	Cartesian coordinates (m)

vortices requires time steps on the order of milliseconds or less [17,18]. As a result, prior simulations of scaling are limited to quasi-steady flow fields [11,20].

Instead of CFD, system-level models of RO often use Sherwood number relationships that estimate the average concentration on the membrane surface [21,22]. That average is useful for predicting the effects of osmotic pressure on permeate production. Spacers, however, generate regions of preferential salt accumulation in which the local concentration far exceeds the average [17,18]. Prior work suggests that scaling likely initiates in these regions [14]. Consequently, for simulations of mineral scaling, a reduced model of spacers should predict both the average and maximum concentration at the membrane surface.

Thus motivated, the current study uses both CFD and bench-scale experiments to propose a reduced model that replaces the Navier–Stokes equations with analytical approximations that mimic the impact of spacers on the velocity field. This focuses the remaining numerical effort on simulating the advection–diffusion equation governing solute transport. The model produces a roughly 10,000-fold reduction in computational effort compared to CFD, and can simulate long channels using a simple Matlab code running on a single computer core. As with Sherwood number relations, the model must be properly fit. While Sherwood relations are often fit to experiments, the current approach must be fit to CFD, because to date, experimental measurements of the concentration fields in RO systems are not available. Once fit, the model provides surprisingly accurate predictions of not only the average and maximum concentration on the membrane, but also the local concentration along the membrane surface. This provides a testbed for exploratory studies of multicomponent mass transport and precipitation for which simulating spacers with CFD is prohibitive.

For this exploratory study, we develop a reduced model using the results of experiments and two-dimensional CFD simulations of spacer filaments with square cross sections oriented tangential to the downstream flow direction, as in Fig. 1(a). These mimic what are called "ladder spacers" [15,23,24]. In contrast, industrial spacers have filaments oriented at oblique angles to the downstream flow [15]. We focus on 2D spacers for three reasons. First, their fluid mechanics are far better understood [25–27]. Second, motivating and validating our model requires a large number of time-resolved CFD simulations for a range of Reynolds numbers and filament arrangements, for which 3D CFD is prohibitively expensive at this exploratory stage. Third, the square filaments match our experiments, in which we 3D print spacers using fused-deposition modeling, for which square filaments can be accurately printed to much high resolution than circular filaments. Overall, our philosophy is that a successful demonstration of a reduced

flow conditions [19]. It must also be stressed that though spacers have a periodic geometry, the flow fields are not themselves periodic in the downstream flow direction, due to the transmembrane permeate flow and the downstream growth of solutal boundary layers. The disparity in length scales consequently cannot be solved by assuming downstream periodicity. The second challenge generated by spacers is a disparity in time scales. Mineral scaling develops over time scales ranging from tens of minutes to several hours. Feed spacers, however, generate unsteady vortex shedding with periods less than one second. Simulating these
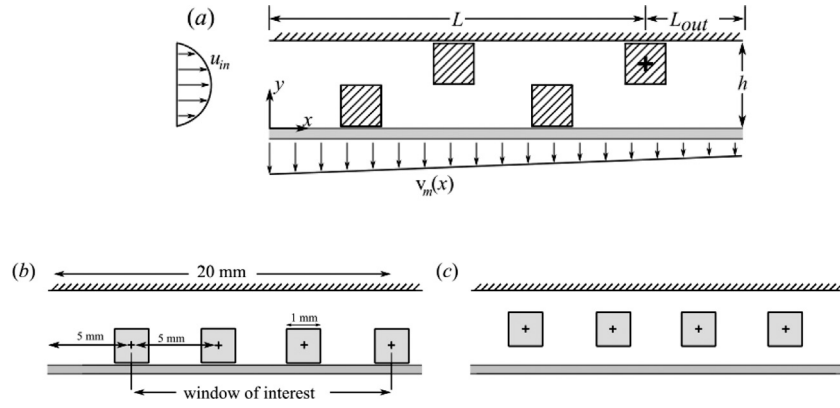
Fig. 1. Sketch (not to scale) of the 2-D plate-and-frame RO system with the (*a*) staggered, (*b*) near-membrane, and (*c*) centerline arrangements.

model for carefully controlled 2D spacers is required before embarking on the much harder 3D problem. Finally, we note that our CFD, experiments, and model all consider a plate-and-frame system with one membrane. We stress, however, that our reduced model can be easily extended to flow between two membranes, as in industrial systems.

The remaining study is organized as follows. Section 2 presents our numerical and experimental methods. Section 3 presents the results of our CFD simulations and experiments. Section 4 uses these results to motivate a reduced model. Section 5 then fits and compares the reduced model with CFD. Section 6 summarizes our conclusions. An additional parametric study of the control parameters in the reduced model is provided as supplemental information.

2. CFD and experimental methods

To motivate our model, we first perform a series of CFD simulations and bench-scale experiments to explore how spacers impact polarization and scaling. Those methods are summarized here.

2.1. Numerical methods

Our CFD considers the incompressible flow of a Newtonian feed solution in a 2D plate-and-frame RO cell of length $L = 20$ mm and height $h = 2$ mm (Fig. 1a). We primarily simulate a solution of water and NaCl. The only exception is in Section 3.2, where we consider a solution that precipitates $CaSO_4$. We discuss those separately in Section 3.2. The feed channel is bounded by a membrane at $y = 0$ and an impermeable plate at $y = h$. Feed enters at $x = 0$ with a uniform concentration C_{in} and mean velocity U_{in}, and exits at $x = L + L_{out}$ with constant pressure P_{out}. We simulate four square filaments (1×1 mm) spaced 5 mm apart in the x-direction, with the first placed 5 mm from the inlet. L_{out} varies with operating conditions to isolate the filaments from outlet conditions. We consider three filament arrangements, all common in prior literature [15]. The staggered arrangement in Fig. 1(*a*) alternates filament centers between $y = 0.55$ and 1.45 mm. This leaves a small gap of 0.05 mm between the filament surface and adjacent membrane or plate. We include this gap because experiments suggest that flow occurs between the membrane and spacer. The inline arrangements in panels (*b*) and (*c*) place all filament centers at $y = 0.55$ (near the membrane) or $y = 1$ mm (on the centerline). We hereinafter refer to the arrangements in panels (*a-c*) as the "staggered", "near-membrane", and "centerline" arrangements, respectively.

Fluid flow and mass transport are governed by the incompressible Navier–Stokes, continuity, and advection–diffusion equations,

$$\rho \left(\frac{\partial \mathbf{v}}{\partial t} + \mathbf{v} \cdot \nabla \mathbf{v} \right) = -\nabla p + \mu \nabla^2 \mathbf{v}, \qquad \nabla \cdot \mathbf{v} = 0, \tag{1}$$

$$\frac{\partial c}{\partial t} + \mathbf{v} \cdot \nabla c = D \nabla^2 c, \tag{2}$$

where $\mathbf{v} = [u \; v]$, p, ρ, and μ are the feed velocity, pressure, density, and viscosity, respectively, and c and D are the solute concentration and mass diffusivity, respectively. Concentration is measured as grams of solute per liter of water. For the lengths considered here, literature shows that the variation of thermophysical properties has negligible impact [14,21]. They are set using the relations in Appendix A, assuming $c = C_{in}$ and $T = 25$ °C.

Feed enters the channel at $x = 0$ with a fully-developed laminar profile and uniform concentration C_{in},

$$u\Big|_{x=0} = U_{in} f(y), \qquad v\Big|_{x=0} = 0, \qquad c\Big|_{x=0} = C_{in}, \tag{3}$$

where U_{in} is the mean inlet feed velocity and

$$f(y) = 6 \left(\frac{y}{h} - \frac{y^2}{h^2} \right), \tag{4}$$

is a parabolic profile with unit mean velocity. At the channel outlet, we apply P_{out}. On the plate and filaments, the flow satisfies the no-slip and no-flux conditions $\mathbf{v} = \mathbf{n} \cdot \nabla c = 0$, where $\mathbf{n}$ is the unit normal. On the membrane, we apply the permeance conditions

$$u\Big|_{y=0} = 0, \qquad v\Big|_{y=0} = -\mathcal{K} \Big[p - \Delta \Pi \Big]_{y=0}, \tag{5}$$

where $\mathcal{K}$ is the membrane permeance and $\Delta \Pi$ is the transmembrane osmotic pressure difference. We set $\mathcal{K} = 11.5$ LMH/bar, which matches the permeance of the membranes in our experiments [28]. We assume no salts permeate the membrane (complete rejection) and approximate the transmembrane osmotic pressure as $\Delta \Pi = \alpha c_m(x)$, where $c_m(x)$ is the local salt concentration on the membrane. Our simulations of NaCl solutions set $\alpha = 77170$ Pa l/g, which agrees with the Pitzer model [29] to within 1% when $c < 100$ g/l. Complete rejection requires the boundary condition

$$\left[vc - D\frac{\partial c}{\partial y} \right]_{y=0} = 0. \tag{6}$$

Modeling incomplete rejection is straightforward [28,30], but beyond our focus.

All numerical methods are detailed in [17]. Eqs. (1)–(2) are discretized to second-order spatial–temporal accuracy using finite-volume, projection, and immersed boundary methods. We set the initial flow fields to the inlet conditions, and integrate in time until the flow reaches a steady-state or transitions to vortex shedding.

2.2. Bench-scale experiments

We explore the impact of spacers on mineral scaling by 3D printing three sets of spacers that match the three spacer arrangements (staggered, near-membrane, and centerline) considered in our CFD simulations (Fig. 1). They are then tested, in triplicate, in a bench-scale system treating a feed that scales $CaSO_4$. The membranes are then
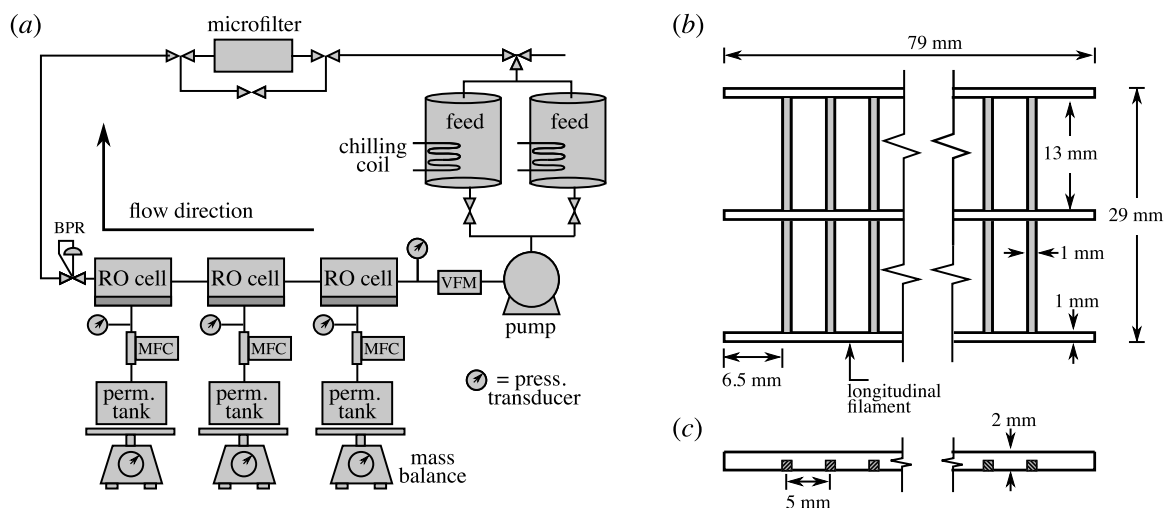
Fig. 2. Panel (*a*) shows a schematic of the bench-scale system. Panels (*b*) and (*c*) show top and side views of the 3D printed spacers, with the transverse filaments shaded gray.

removed and photographed to determine where scale formed, and how that compares with CFD predictions of the local concentration $c_m(x)$ along the membrane.

The bench-scale system (Fig. 2) stores feed in two tanks at 25 °C. One contains DI water, while the second contains the scaling solution. The flow rate exiting the tanks is set by a diaphragm pump with a pulse dampener (Hydra-Cell, Wanner Engineering Inc., Minneapolis, MN), and measured by a volumetric flow meter (Macnaught, Tampa, Florida). The feed passes through three stainless steel, plate-and-frame, RO cells fabricated in-house. The feed pressure exiting the last cell is set by a backpressure regulator (Swagelok, Solon, OH), and then passes through an activated carbon microfilter with a pore size of 0.5 μm (Cole Parmer, Vernon Hills, IL) to remove any solids or precipitates before returning the retentate to the feed tank. The permeate pressure of each cell is measured by single-end pressure transducers (Omega Engineering). The permeate flow rates of each cell are individually controlled using mass flow controllers (Bronkhorst, Bethlehem, PA). Temperature, conductivity, and pH are measured throughout the experiment using probes by Thermo Scientific (Waltham, MA). The composition of the feed was also determined by measuring anion concentrations using ion chromatography (Dionex ICS-2100, Thermo Scientific).

Each cell has a feed channel of 80 mm length, 30 mm width, and 2 mm height. Membrane coupons harvested from a DOW-XLE 4040 module are presoaked in 25 vol % aqueous isopropyl alcohol for 30 min prior to loading in the cells. Prior to each experiment, DI water is circulated through the system for 20 min to remove particulates. DI water is then recirculated for one hour to measure the coupons' permeance. Aqueuos solutions of sodium sulfate and calcium chloride (Sigma Aldrich, St. Louis) are then added as concentrated aqueous solutions to the second feed tank to produce an aqueous solution of 2380 ± 40 ppm sodium sulfate and 1860 ± 30 ppm calcium chloride (concentrations are an average of measurements from multiple experiments; variations represent one standard deviation). The feed pH is adjusted to 6.8 using NaOH. The resulting feed is slightly undersaturated in gypsum, with a saturation index of $\log(IAP/K_{sp}) = -0.03$, where IAP is the ion activity product and K_{sp} is the solubility product. The index was computed using the open-source software PHREEQC [31]. After the source is switched to the feed solution, the initial 3 L of retentate is discarded to account for dilution by residual DI. The experiments are run with constant permeate flux, such that scale formation produces an increase in transmembrane pressure. The permeate and retentate are returned to the feed tank to maintain approximately constant feed concentration. Following each experiment, the system is rinsed with DI water for 2 min before disassembling the cells and removing the membranes, which are dried in ambient conditions.

The printed spacers (Fig. 2b) have three longitudinal filaments that divide the feed channel into two parallel ducts. Each duct has 14 transverse filaments spaced 5 mm apart. No transverse filaments were printed within 6.5 mm of the inlet/outlet to avoid interfering with flow entering/exiting through the steel plate opposite the membrane. The spacers have a length of 79 mm and width of 29 mm, to fit in the feed channel without warping. All spacers are manufactured using a Stratasys F170 FDM printer with acrylonitrile butadiene styrene. Each arrangement was tested in triplicate by printing three identical spacers and running them simultaneously in the three RO cells.

3. CFD and experimental results

Here we summarize the CFD and experimental results that motivate our model. The CFD results in Section 3.1 show that spacers generate local maxima in concentration on the membrane. The experimental results in Section 3.2 show that these maxima are what trigger scaling.

3.1. CFD results

To investigate the impact of spacers on the flow fields, we set C_{in} = 2 g/l NaCl and P_{out} = 8.618 bar (125 psig). This mimics the treatment of a low-concentration brackish water using the membrane in our experiments. For each filament arrangement, we perform ten simulations between $50 \leq Re \leq 500$, where $Re = \rho U_{in} h / \mu$. These require 0.0224 m/s $\leq U_{in} \leq$ 0.224 m/s.

Fig. 3 shows results for the near-membrane arrangement. Panel (*a*) shows streamlines when $Re = 50$, panel (*b*) shows the corresponding concentration $c_m(x)$ on the membrane, and panel (*c*) shows the permeate velocity $v_m(x)$, defined as positive when permeate leaves the channel. Distances are normalized with h, concentrations are normalized with C_{in}, and v_m is normalized with U_{in}. Results are presented in the window-of-interest $2.5 \leq x/h \leq 10$ between the first and last filament. Panel (*a*) shows that filaments generate clockwise rotating vortices whose impact on polarization can be interpreted by the paths sketched in panel (*a*). Path i–ii brings low concentration feed to the membrane, generating a concentration minimum upstream of the filament. As feed flows upstream along path ii–iii, its concentration increases due to permeate extraction through the membrane. This brings high-concentration fluid to the maximum just downstream of a filament.

To measure the risk of mineral scaling, we define C_{max} as the maximum concentration in the window of interest 5 mm $\leq x \leq$ 20 mm. In all cases, C_{max} occurs on the membrane surface. The solid line in Fig. 3(*d*) shows that for the near-membrane arrangement, C_{max} tends
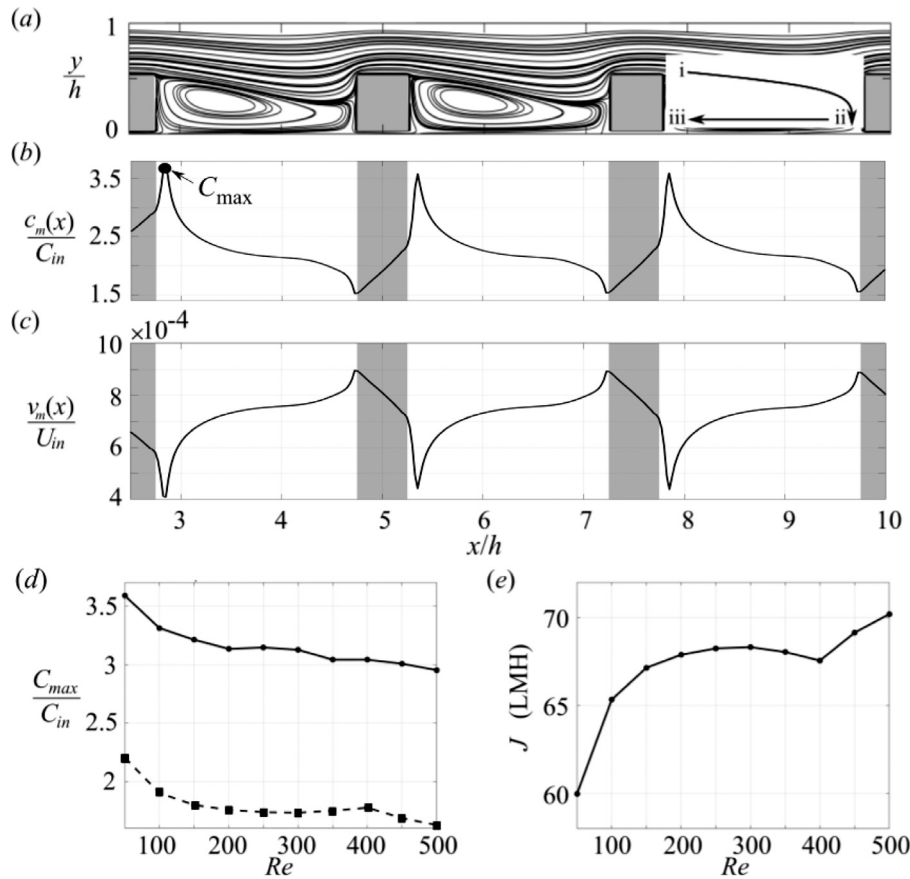
Fig. 3. CFD results for the near-membrane arrangement. (*a*) Streamlines when $Re = 50$. (*b*) Salt concentration $c_m(x)$ on the membrane surface, normalized with C_{in} when $Re = 50$. (*c*) Local permeate velocity $v_m(x)$ normalized with U_{in} when $Re = 50$. The downstream positions of the spacers are shaded gray. (*d*) Variation of C_{max} (solid dots) and C_{osm} (squares) with Re. (*e*) Variation of J with Re.

to decrease with increasing Reynolds number. Though NaCl is a major source of osmotic pressure in feed waters, it precipitates at around 360 g/l. Mineral scaling typically occurs due to sparingly soluble salts, such as $CaSO_4$, which precipitate below 3 g/l [14,32]. Though we simulate NaCl, we expect sparingly soluble salts will produce similar results, because their mass diffusivities D are similar to that of NaCl [33].

To measure the impact of spacers on permeate production, we compute the permeate flux J produced in the window of interest,

$$J = \frac{1}{15\,\text{mm}} \int_{5\,\text{mm}}^{20\,\text{mm}} v_m(x)\,dx. \tag{7}$$

We report J in LMH. Fig. 3(*e*) shows that J increases with Reynolds number up to $Re = 300$. This occurs due to an increase in vortex strength, which reduces the time that fluid parcels spend along path ii–iii near the membrane. The decrease in J between $300 < Re < 400$ occurs due to the appearance of secondary vortices that generate low-velocity stagnation points near the membrane.

Experimental studies often report an average concentration C_{osm} defined through the relation [28]

$$J = \mathcal{K}\left(P_{out} - \alpha C_{osm}\right). \tag{8}$$

The concentration C_{osm} produces the same average osmotic pressure as $c_m(x)$, which explains the subscript "*osm*". Consequently, a decrease in C_{osm} always produces an increase in J, and vice versa. This is demonstrated by the dashed line in Fig. 3(*d*), which shows that C_{osm} decreases with Reynolds number, as J increases with Reynolds number. Comparing C_{max} and C_{osm} for the near-membrane arrangement, we see C_{osm} underestimates C_{max} by over 100 %, and consequently underestimates the risk of mineral scaling. It is tempting to conclude that C_{max} and C_{osm} differ by a nearly constant value, but otherwise vary similarly

with Reynolds number. If that were true, we could try to predict C_{max} through some linear relation of the form $C_{max} = a_1 C_{osm} + a_2$, where a_1 and a_2 are constant coefficients. We will see, however, that the other arrangements produce very different behaviors for C_{osm} and C_{max}.

Fig. 4(*a*) shows streamlines for the staggered arrangement when $Re = 50$. Panel (*b*) shows that vortical structures generate local maxima in $c_m(x)$ both upstream and downstream of the filaments near the membrane. Meanwhile, acceleration of the flow beneath the filaments on the plate generates local minima. Comparing the results for C_{max} (solid line) and C_{osm} (dashed line) in Fig. 4(*c*), we see that these two quantities now vary quite differently with Reynolds number. Note that for the staggered arrangement, we modify the window-of-interest to $5 \leq x/h \leq 10$ (between the second and fourth spacers), because inlet effects impact the concentration field near the first filament at higher Reynolds numbers. This is evident in Fig. 12(*c*), in which the solid line shows CFD results at $Re = 300$.

Fig. 5 shows streamlines for the centerline arrangement when $Re = 50$ (panel *a*) and $Re = 200$ (panel *b*). Panel (*c*) shows the corresponding concentrations $c_m(x)$. In both cases, acceleration of the flow beneath the filaments decreases the local membrane concentration. Above the critical Reynolds number $Re_c = 110$, a transition to unsteady vortex shedding generates small vortices that travel along the membrane. These generate concentration maxima roughly mid-distance between filaments. Fig. 5(*d*) shows that this causes C_{max} (solid line) to increase between $Re = 150$ and 250. Above $Re = 250$, the increased strength of the near-membrane vortices ejects solutes away from the membrane, decreasing C_{max}. Note that despite the unsteady flow above Re_c, the concentration $c_m(x)$ remains nearly steady, oscillating less than 1%. Comparing the results for C_{max} (solid line) and C_{osm} (dashed line) in panel (*d*), we stress that these two quantities vary quite differently with Reynolds number.
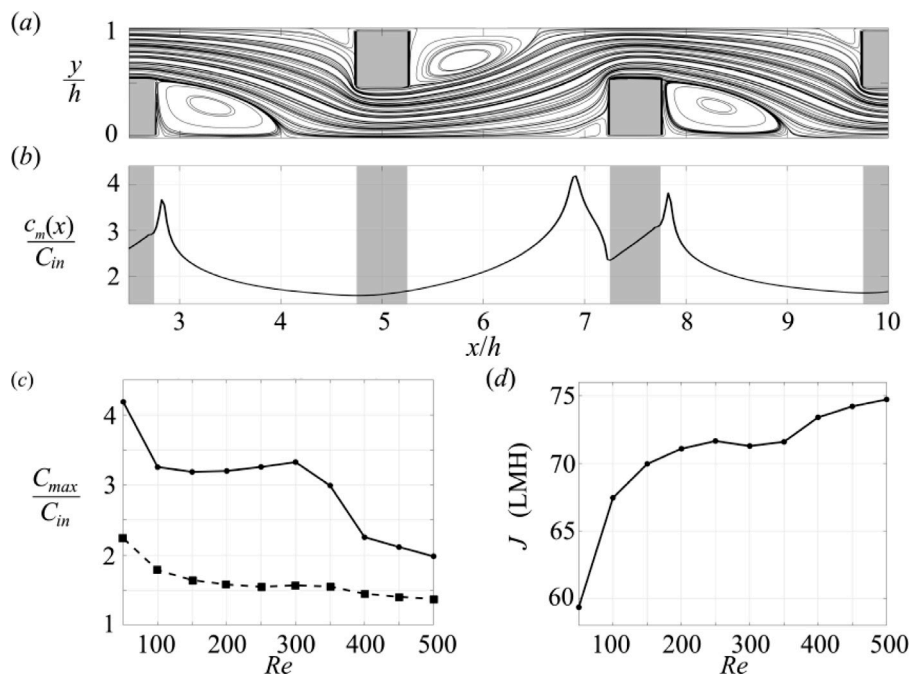
Fig. 4. CFD results for the staggered arrangement. (a) Streamlines when $Re = 50$. (b) $c_m(x)$ on the membrane surface, normalized with C_{in} when $Re = 50$. The downstream positions of the spacers are shaded gray. (c) Variation of C_{max} (solid dots) and C_{osm} (squares) with Re. (d) Variation of J with Re.
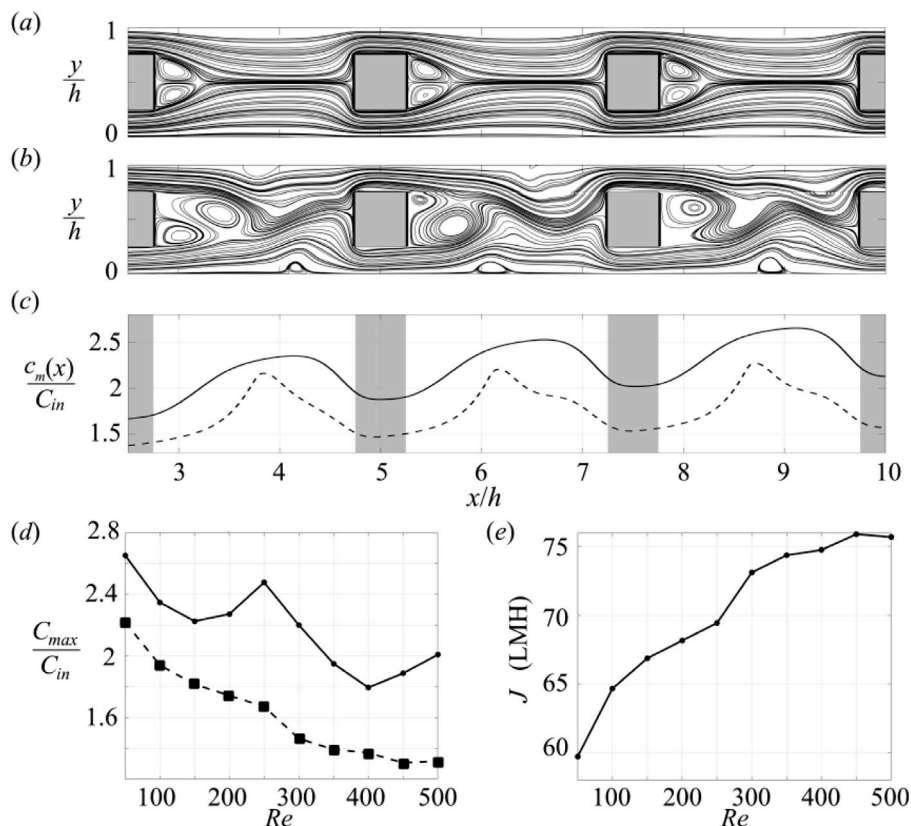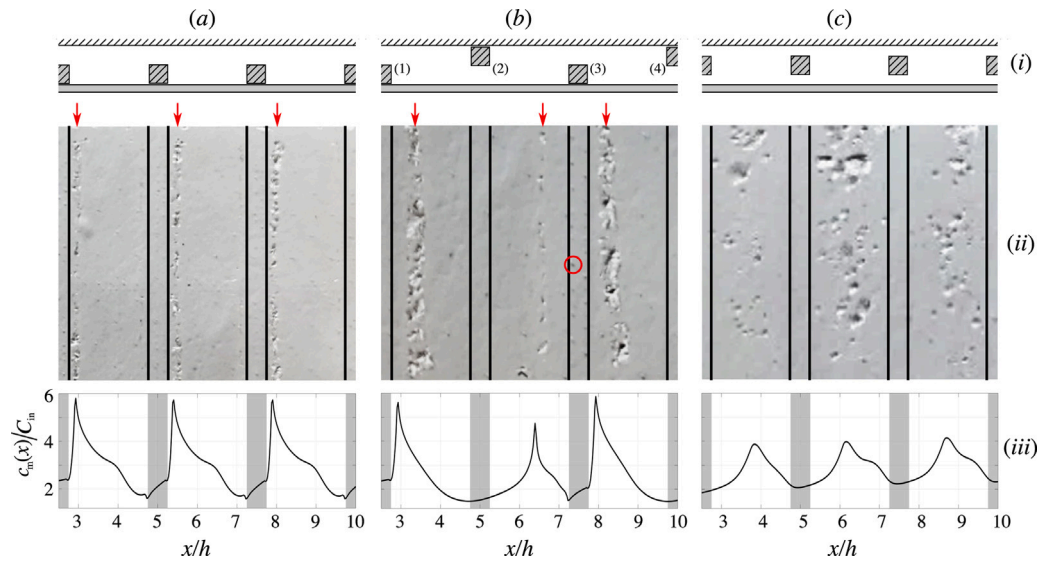

Fig. 5. CFD results for the centerline arrangement. (a) Streamlines when $Re = 50$. (b) Streamlines when $Re = 200$. (c) Concentration $c_m(x)$ when $Re = 50$ (solid line) and when $Re = 200$ (dashed line). The downstream positions of the spacers are shaded gray. (d) Variation of C_{max} (solid dots) and C_{osm} (squares) with Re. (e) Variation of J with Re.

3.2. Experimental results

Fig. 6 shows photographs (row *ii*) of membranes that experienced CaSO$_4$ scaling in our experiments. All experiments were run using the outlet pressure $P_{out} = 16$ bar and inlet Reynolds number of $Re =$ 200. The vertical black lines show the approximate positions of four filaments. These are estimated by marking the membrane when it is removed from the cell. In some cases, the filaments also left small indentations on the membrane surface, which helped us estimate their positions. The red circle in panel (*b*) shows one such indentation. The

Fig. 6. Experimental and CFD results for the near-membrane (*a*), staggered (*b*), and centerline (*c*) arrangements. For each panel, row (*i*) shows the arrangement, row (*ii*) shows a photograph of the membrane, and row (*iii*) shows the CFD predictions for $c_m(x)/C_{in}$. The black lines in row (*ii*) show the approximate positions of the filaments. The red arrows in panels (*a*) and (*b*) show bands of precipitation. The red circle in panel (*b*) shows an indentation on the membrane from the spacer filament.

distribution of mineral scaling in the photographs are representative of what we observed over the full membranes, excluding the near inlet/outlet regions. SEM and EDX analysis confirmed the structure and chemical composition of the scale on the membrane surface. SEM images of the scaled membrane displayed the rosette structure indicative of gypsum surface crystallites [34]. This confirms that the deposition of crystallites formed in the bulk solution was minimal due to filtration of the feed solution. EDX analysis confirmed the presence of calcium and sulfur in the scale. In our discussion below, we compare the photographs in terms of where precipitation formed, but not the amount of precipitation, because the photographs come from separate experiments that were stopped at different times. We do not compare experimental and CFD results for the average permeate production, because the CFD considers only a small segment of the bench-scale flow cell. Moreover, the experiments include mineral scaling, which is not included in the CFD.

To compare with CFD, we follow the procedure of Lyster and Cohen [14], which sets $D = 1.23 \times 10^{-9}$ m^2/s. We set the osmotic pressure coefficient to $\alpha = 46326$ Pa l/g, which was computed using OLI software [35]. Row (*iii*) of Fig. 6 shows the resulting CFD predictions for the salt concentration $c_m(x)$ on the membrane, between the four filaments in our simulations. Comparing the experimental and CFD results for the near-membrane arrangement (panel *a*), we see that scale formed along thin bands immediately downstream of each filament. These bands are marked with red arrows. This agrees with the CFD prediction of a sharp peak in $c_m(x)$ behind each filament.

To facilitate our discussion of the staggered arrangement, we have labeled the four filaments as (1)-(4) in panel (*b*). We see that scale formed in thick bands downstream of filaments (1) and (3), where CFD predicts $c_m(x)$ is maximized. We also see a thin band of crystals upstream of filament (3), which agrees with the CFD prediction of a smaller secondary maximum in $c_m(x)$. We see no scaling below filament (2), where CFD predicts $c_m(x)$ is minimized. Finally, turning our attention to the centerline arrangement in panel (*c*), we first note that scaling is minimized beneath the filaments, where CFD predicts $c_m(x)$ is minimized. Between downstream filaments, the scale is not concentrated along sharp bands. This is likely explained by the CFD prediction that the centerline arrangement does not produce sharp peaks in concentrations, like those observed for the near-membrane and staggered arrangements.

4. Reduced-order model

The reduced model replaces the Navier–Stokes equations with analytical expressions that mimic the impact of spacers on the velocity field. For that, the model decomposes the velocity field as

$$\mathbf{v} = \mathbf{v}_b(x, y) + \mathbf{v}_p(x, y), \tag{9}$$

where we refer to $\mathbf{v}_b$ as the *base flow* and $\mathbf{v}_p$ as the *perturbation*. We stress that though we borrow these terms from perturbation theory, we do not require $\mathbf{v}_p$ to be small, and we do not perform a perturbation expansion. Rather, we lump the physics of the membrane permeance condition (5) into the base flow, and model the spacers through $\mathbf{v}_p$, as detailed below. We furthermore show that while $\mathbf{v}_b$ is not periodic, the perturbation flow $\mathbf{v}_p$ can be. The model also approximates the flow as steady, even when CFD produces unsteady shedding.

4.1. Base flow

The base flow approximates a 2D plate-and-frame RO system without spacers (Fig. 7a). Approximations for that case are well established [36–40], and come from the pioneering work of Regirer [41]. The approximation should not be confused with that of Berman [42], which assumes a constant permeate velocity. We first approximate the downstream velocity u_b as

$$u_b = U(x)f(y), \tag{10}$$

where $U(x)$ is the local mean feed velocity, and $f(y)$ is the parabolic profile (4). Conservation of mass then requires $dU/dx = -v_m(x)/h$ and

$$v_b = v_m(x)s(y), \quad s(y) = \frac{3y^2}{h^2} - \frac{2y^3}{h^3} - 1. \tag{11}$$

Note that $s(0) = -1$, because $v_m(x)$ is defined as positive when permeate leaves the system. We determine $v_m(x)$ by applying the membrane condition

$$v_m(x) = \mathcal{K}\left[P_{out} - \alpha c_m(x)\right], \tag{12}$$

where we approximate the local transmembrane pressure as P_{out}.

Using the base-flow, we can solve the steady advection–diffusion equation,

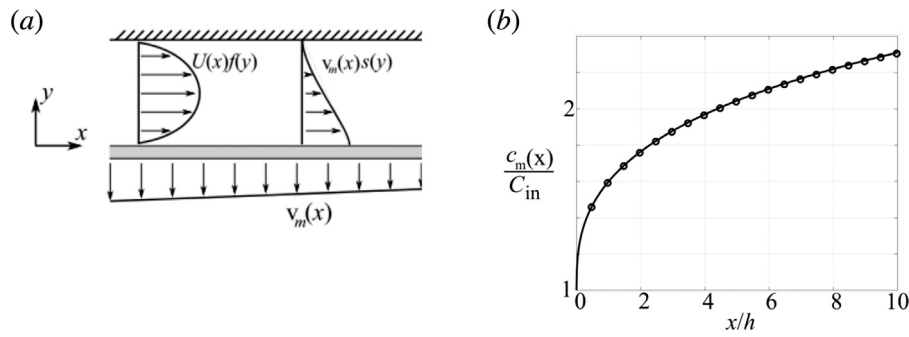$$\mathbf{v}_b \cdot \nabla c = \mathcal{D}\nabla^2 c, \tag{13}$$

Fig. 7. (a) Sketch (not to scale) of the base-flow. (b) Comparison of the base flow (circles) and CFD (solid lines) predictions of $c_m(x)$ when $Re = 200$ $C_{in} = 2$ g/l NaCl, $P_{out} = 8.618$ bar (125 psi). CFD is performed without spacer filaments.
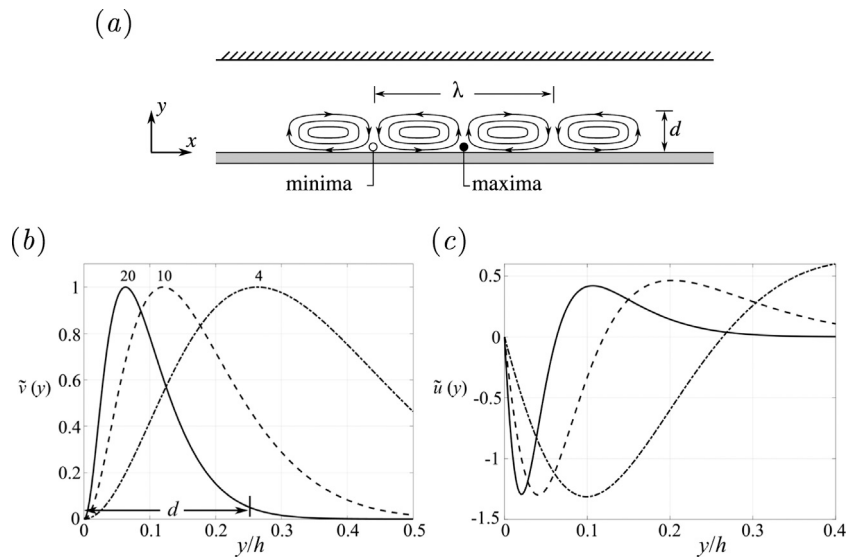

Fig. 8. (a) Conceptual sketch (not to scale) of the vortical perturbations. (b) Perturbation profile $\tilde{v}(y)$ when $\lambda = 2\pi$, and $b = 4$ (dash-dotted lines), $b = 10$ (dashed lines), and $b = 20$ (solid line). (c) Corresponding profiles for $\tilde{u}(y)$.

using a simple fixed-point iteration. Using the initial velocity field $u_b = U_{in} f(y)$ and $v_b = 0$, we solve Eq. (13) subject to the condition that there is no salt transport through the membrane

$$\left[v_b c - D \frac{\partial c}{\partial y} \right]_{y=0} = 0, \tag{14}$$

and remaining boundary conditions detailed in Section 2.1. Using the resulting concentration $c_m(x)$, we then solve Eqs. (10)–(12) for an updated $\mathbf{v}_b$. We repeat this procedure until $c(x, y)$ no longer varies with subsequent iterations. Fig. 7(a) shows the base flow predictions (circles) for $c_m(x)$ when $C_{in} = 2$ g/l NaCl, $P_{out} = 8.618$ bar (125 psi), and $Re = 200$. We see excellent agreement with CFD (solid lines) performed without spacers.

4.2. Perturbation flow

Our CFD shows that vortical flow structures play an important role in polarization for all arrangements, except the centerline arrangement when $Re < 110$. This suggests that spacers could be modeled by setting the perturbation to a periodic array of counter-rotating vortices, as in Fig. 8(a). These generate minima in $c_m(x)$ where adjacent vortices bring low-concentration bulk fluid to the membrane. Maxima occur where downstream and upstream advection of high-concentration feed along the membrane surface meet.

In an attempt to model all three spacer arrangements using a common perturbation velocity field, we seek an expression that controls the downstream wavelength λ and membrane-normal thickness d of

the vortices. To control λ, we express $\mathbf{v}_p$ as a Fourier mode in the x-direction,

$$u_p = A \tilde{u}(y) \sin\left(\frac{2\pi x}{\lambda} \right), \qquad v_p = A \tilde{v}(y) \cos\left(\frac{2\pi x}{\lambda} \right). \tag{15}$$

where conservation of mass requires $\tilde{u} = -(d\tilde{v}/dy)\lambda/(2\pi)$. The shape-function $\tilde{v}(y)$ controls the perturbation profile in y, and is defined to have an absolute maximum $\|\tilde{v}\|_\infty = 1$, so that A sets the perturbation amplitude. To control the vortex structure in the y-direction, we impose three constraints. **(i)** $\tilde{v}(y)$ should have a maximum in the interval $0 < y < d$ and tend to zero in the region $y > d$. **(ii)** We enforce no-slip ($u_p = 0$) on the membrane by imposing $\tilde{v}'(0) = 0$. **(iii)** To simplify the coupling between $\mathbf{v}_b$, $\mathbf{v}_p$, and c on the membrane, we force $v_p = 0$ at $y = 0$. This allows us to solve the steady advection–diffusion equation

$$\left(\mathbf{v}_b + \mathbf{v}_p \right) \cdot \nabla c = D \nabla^2 c, \tag{16}$$

subject to the condition that there is no salt permeation through the membrane

$$\left[v_b c - D \frac{\partial c}{\partial y} \right]_{y=0} = 0, \tag{17}$$

where v_b satisfies the permeance condition (12),

$$v_b \big|_{y=0} = -\mathcal{K} \left[P_{out} - \alpha c_m(x) \right]. \tag{18}$$

Though subtle, this reduced coupling is a key feature of our model. From a numerical perspective, it lets us solve Eq. (16) using the same fixed point iteration detailed in Section 4.1. Using a computer with
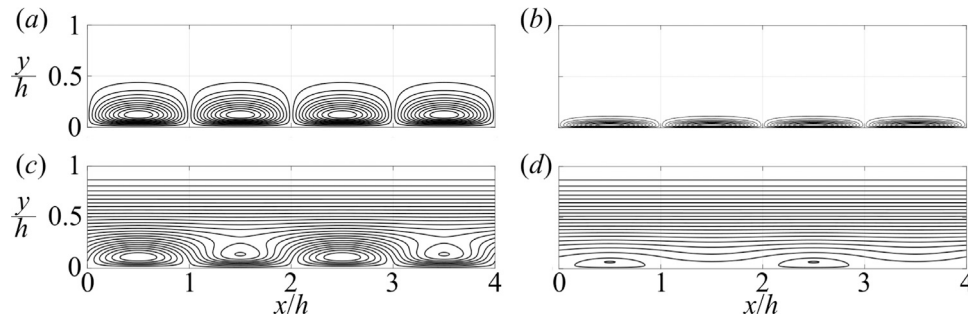
Fig. 9. Panels (*a*) and (*b*) show streamlines generated by $\mathbf{v}_p$ when $\lambda = 2h$ and $b = 10$ (panel *a*) and $b = 50$ (panel *b*). Panels (*c*) and (*d*) show the net flow $\mathbf{v} = \mathbf{v}_b + \mathbf{v}_p$ when $\lambda = 2h$, $b = 10$, and $A = 1$ (panel *c*) and $A = 0.1$ (panel *d*).

Intel Xeon Gold 6238R processors, the CFD simulations on a single core take between two to seven days to run to completion. On the same computer, the reduced model requires roughly 1 min, representing a 1000 to 10,000-fold speed up. From a physical standpoint, $\mathbf{v}_p$ perturbs solute advection through Eq. (16), which generates oscillations in $c_m(x)$. Eq. (18), however, assumes that oscillations in $v(x, y)$ vary normal to the membrane like $s(y)$. This lumps the impact on permeate production into $\mathbf{v}_b$ rather than $\mathbf{v}_p$. That is what allows us to approximate $\mathbf{v}_p$ as periodic in x. Section 5.1 shows that this reduced coupling reproduces CFD results to surprising accuracy.

Though an infinite number of potential shape-functions $\widetilde{v}(y)$ are possible, one convenient family takes the form.

$$\widetilde{v}(y) = \frac{y}{B} \sin\left[\pi \left(1 - \frac{y}{h}\right)^b\right], \tag{19}$$

where $b > 0$ controls the thickness, and B normalizes $\widetilde{v}(y)$ so its maximum value is always unity. This family is built by first recognizing that the function $\widetilde{v} = \sin(\pi y/h)$ produces one half of a sine wave as y varies from 0 to h. That satisfies the no-penetration condition at $y = 0$ and h, but does not satisfy the no-slip condition $\widetilde{v}'(0) = 0$. We consequently modify the function as $\widetilde{v} = y \sin(\pi y/h)$. Next, to control where the maximum of $\widetilde{v}$ occurs, we replace the argument $\pi y/h$ in the sine function with $\pi (1 - y/h)^b$. Fig. 8(*b*) shows $\widetilde{v}(y)$ when $b = 4$ (dash-dotted lines), $b = 10$ (dashed lines), and $b = 20$ (solid lines). Panel (*c*) shows the corresponding $\widetilde{u}(y)$. Note how increasing b pushes the maximum of $\widetilde{v}$ closer to the membrane, decreasing the thickness of the vortical structures. If we define d as the y-location where $\widetilde{v}(d) = 0.05$, then d is well approximated by

$$d = \begin{cases} 1.137 - 0.122b + 0.00646b^2 - 0.000128b^3, & b \leq 20, \\ 4.52b^{-0.95}, & b \geq 20. \end{cases} \tag{20}$$

Fig. 9 shows streamlines generated by $\mathbf{v}_p$ when $\lambda = 2h$ and $b = 10$ (panel *a*) and $b = 50$ (panel *b*). Panels (*c*) and (*d*) show the net flow $\mathbf{v} = \mathbf{v}_b + \mathbf{v}_p$ when $b = 10$ and $A = 1$ (panel *c*) and 0.1 (panel *d*). These show that the penetration of the vortices into the channel also increases with the amplitude A.

5. Reduced model results

The reduced model is controlled by A, b, and λ. Unless otherwise stated, we set $\lambda = 5$ mm to match the filament spacing in our CFD. That leaves two parameters (A and b) that can be varied to match the results of CFD. In practice, we first performed a parametric study to elucidate the physical significance of A and b. For brevity, that analysis is provided in the supplemental information, and we focus on the fitting here. Throughout, we set $C_{in} = 2$ g/l NaCl and $P_{out} = 8.618$ bar (125 psi). We set the system length to $L = 20$ mm, except in Section 5.3, where we model the long system $L = 400$ mm.

5.1. Fitting to CFD

For a given Reynolds number, we fit the reduced model to the CFD by finding the combination of A and b that minimize the weighted error

$$E = E_J + E_C + w|E_J - E_C|, \tag{21}$$

$$E_J = \frac{|J^{mod} - J^{CFD}|}{J^{CFD}}, \qquad E_C = \frac{|C_{max}^{mod} - C_{max}^{CFD}|}{C_{max}^{CFD}}. \tag{22}$$

The term E_J measures the difference between the model prediction for the net permeate flux (J^{mod}) and the CFD result (J^{CFD}). The term E_C similarly measures the difference between the model and CFD predictions for C_{max}. The coefficient w is an error penalty coefficient introduced so that E is minimized when $E_J = E_C$. Otherwise, E_C is often minimized at the expense of E_J. We found that setting $w = 1$ minimizes E_J and E_C simultaneously.

Fig. 10 shows the fitting for the near-membrane arrangement. Panel (*a*) compares the CFD and model results for C_{max} and C_{osm}, while panel (*b*) compares results for J. The model reproduces the CFD results to within a relative error below 3%. Fig. 10(*c*) compares the CFD and model predictions for $c_m(x)$ when $Re = 200$. The model reproduces the spatial variation of $c_m(x)$ remarkably well, though this was not necessarily our objective. The fitting data for each spacer arrangement is provided in Appendix B.

Fig. 11(*a*–*b*) compares the model and CFD results for C_{max}, C_{osm}, and J for the centerline arrangement. For $Re \geq 250$, A and b can be set to reproduce the CFD results for C_{max}, C_{osm} and J very well, with errors on the order of 1% or less. For $Re \leq 200$, the errors in model predictions range from 8% at $Re = 50$ to 3% at $Re = 200$. Physically, this can be explained by the CFD prediction that vortical structures do not appear on the membrane until $Re_c = 110$. The strength and thickness of these vortices then increase with Re. It is important to recall that, while the CFD is unsteady for $Re \geq Re_c$, the reduced model is steady in all cases. Fig. 11(*c*) compares the CFD and model predictions for $c_m(x)$ when $Re = 250$. The model (dashed line) matches the magnitude of the peaks of $c_m(x)$, but with a spatial phase shift from the CFD prediction (solid line). This is easily corrected in the model by modifying Eq. (15) to include a phase shift, x_0, in $\cos(2\pi/\lambda(x - x_0))$. Setting $x_0 = 2$ mm produces the dashed–dotted line in Fig. 11(*c*).

Fig. 12(*a*–*b*) compares the model and CFD results for C_{max}, C_{osm}, and J for the staggered arrangement. The maximum relative error is less than 7%. Recall that for this arrangement, we modify our window-of-interest to $5 \leq x/h \leq 10$. Focusing on that window, the model over-predicts the concentration peaks upstream of the spacer on the membrane, which may explain why the model under-predicts J in Fig. 12(*b*) for $Re \leq 400$. Note that unlike the centerline and near-membrane arrangements, the staggered arrangement is periodic over $\lambda = 10$ mm. We repeated our fitting procedure using $\lambda = 10$ mm, but found nearly identical results for C_{max} and J as obtained with $\lambda = 5$ mm. The dashed–dotted line in Fig. 12(*c*) shows $c_m(x)$ obtained using $\lambda = 10$ mm. This produces only one peak in concentration in the window-of-interest compared with the two that appear when $\lambda = 5$ mm.
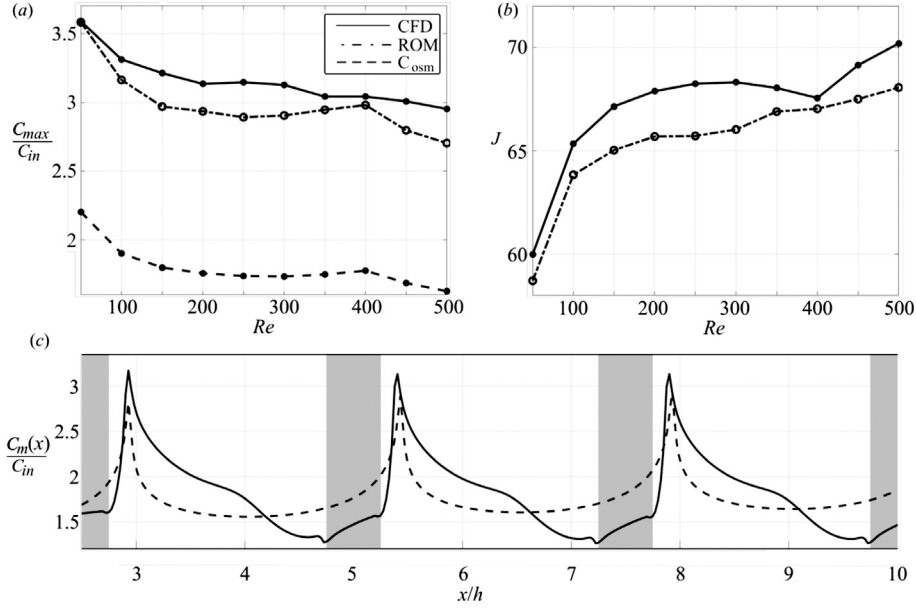
Fig. 10. Model and CFD results for the near-membrane arrangement. (*a*) Comparison of CFD results for C_{max} (solid dots) and C_{osm} (solid squares) with model predictions for C_{max} (open circles) and C_{osm} (open squares). (*b*) Comparison of CFD (solid dots) and model (open circles) predictions for J. (*c*) Concentration at the membrane surface, $c_m(x)$, predicted by CFD (solid line) and the model (dashed line) when $Re = 200$.
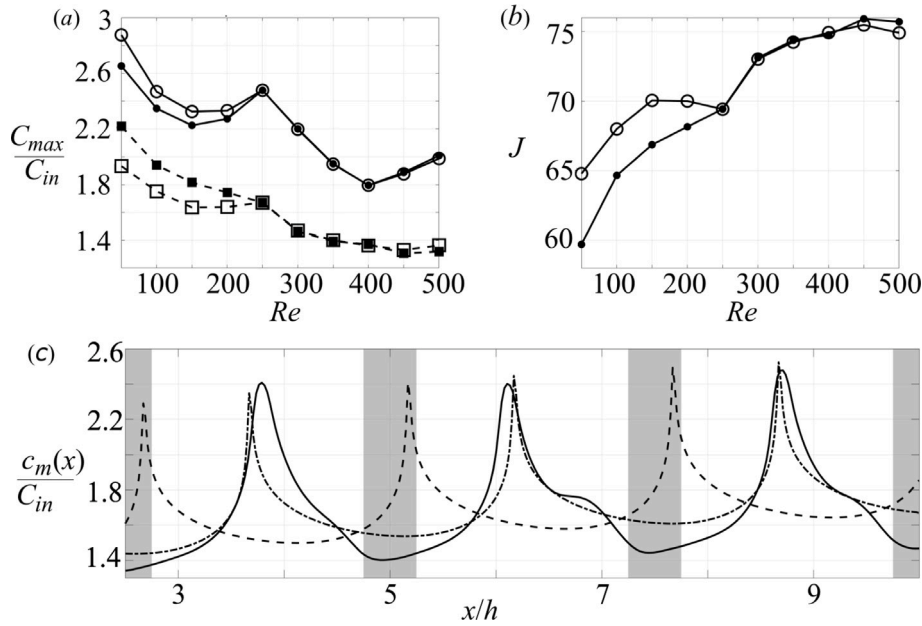
Fig. 11. Model and CFD results for the centerline arrangement. (*a*) Comparison of CFD results for C_{max} (solid dots) and C_{osm} (solid squares) with model predictions for C_{max} (open circles) and C_{osm} (open squares). (*b*) Comparison of CFD (solid dots) and model (open circles) predictions for J. (*c*) Membrane concentration $c_m(x)$ predicted by CFD (solid line) and the model (dashed line) when $Re = 250$. The dash-dotted line shows the model results with a 2 mm phase shift.

5.2. Alternate perturbation structure

Reduced models could be further improved by tailoring the perturbation fields to CFD data. For demonstration, we develop a velocity perturbation $\mathbf{v}_p$ tailored to the centerline arrangement at subcritical flow, $Re < 110$. Fig. 5(*a*) shows that in this case, there are no vortical structures on the membrane, and the vortical perturbation developed in Section 4.2 is less physical. To motivate a new perturbation, Fig. 13(*b*) shows a colormap of the CFD result for

$$u^* = u(x, y) - U_{in}, \qquad Re = 50, \tag{23}$$

between the second and third spacers, $4.75 \le x/h \le 7.25$. The quantity u^* can be interpreted as the perturbation to u generated by the spacers.

The solid line in panel (*a*) shows the corresponding CFD result for the gradient

$$\gamma(x) = \left.\frac{\partial u^*}{\partial y}\right|_{y=0}. \tag{24}$$

The solid line in panel (*c*) shows the variation of u^* with y at $x/h = 7$, which is marked with a red line in panel (*a*). Overall, the spacers accelerate the flow near the membrane such that u^* and $\partial u^*/\partial y$ are always positive near $y = 0$. Meanwhile, to conserve mass, u^* is negative near the centerline. We consequently seek an expression for u_p in the form

$$u_p(x, y) = \gamma(x)\left[a_0 + a_1\hat{y}^2 + a_2\hat{y}^4\right], \qquad \hat{y} = y - \hat{h}, \tag{25}$$
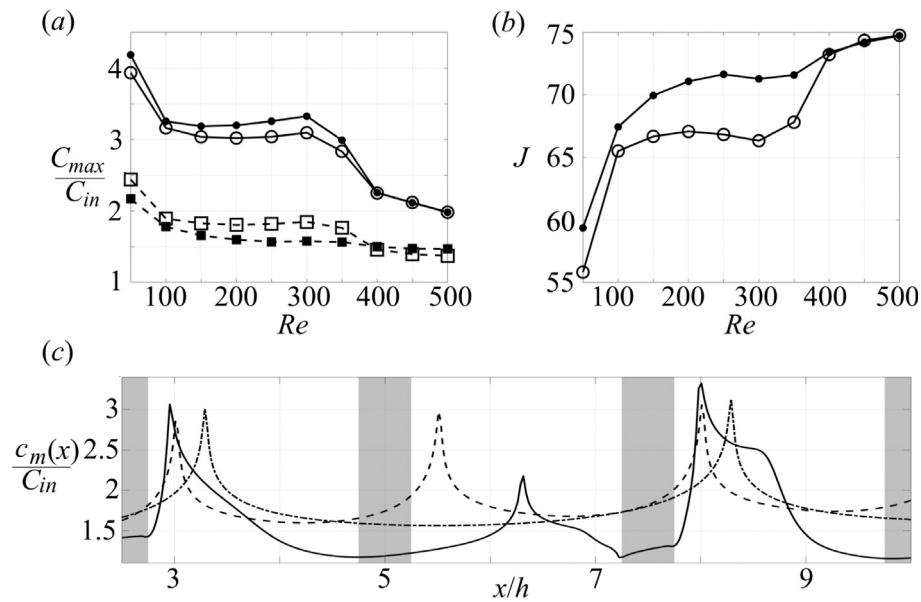
Fig. 12. Model and CFD results for the staggered arrangement. (a) Comparison of CFD results for C_{max} (solid dots) and C_{osm} (solid squares) with model predictions for C_{max} (open circles) and C_{osm} (open squares). (b) Comparison of CFD (solid dots) and model (open circles) predictions for J. (c) Comparison of $c_m(x)$ produced by the reduced model (dashed line) and CFD (solid line) for the staggered arrangement at $Re = 300$. The dashed–dotted line shows reduced model results obtained using $\lambda = 10$ mm.
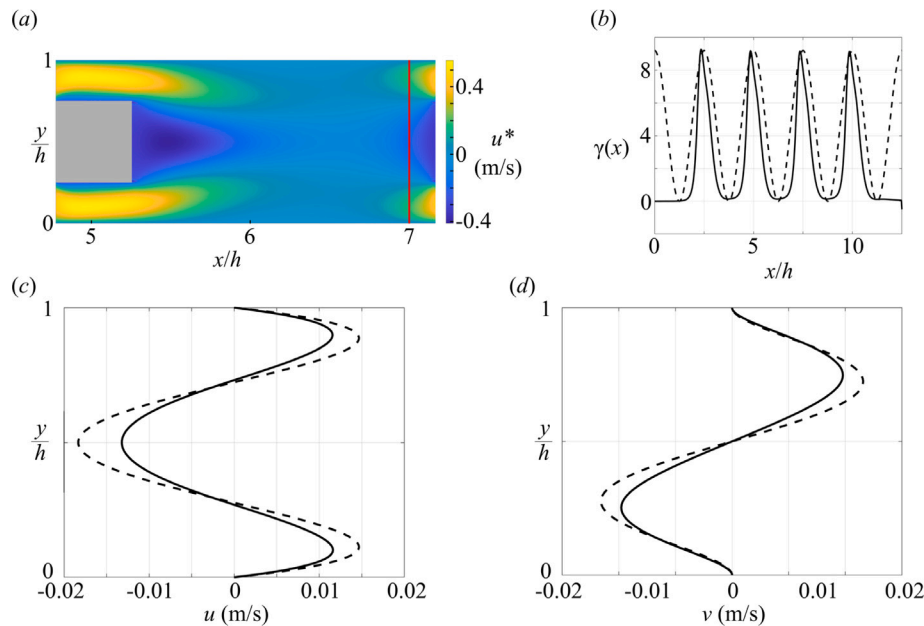
Fig. 13. (a) Colormap of $u^* = u - U_{in}$ extracted from CFD for the centerline arrangement when $Re = 50$. (b) Comparison of the gradient $\gamma(x)$ on the membrane surface for CFD and proposed model using $G = 2.3$ and $\beta = 1$. (c) CFD (solid line) and model (dashed line) prediction for u^* at $x/h = 7$ (red line in panel a). (d) CFD (solid line) and model (dashed line) prediction for v at $x/h = 7$ (red line in panel a). (For interpretation of the references to color in this figure legend, the reader is referred to the web version of this article.)

where $\hat{h} = h/2$. This leverages symmetry to approximate u_p as an even function about the centerline. To determine the coefficients a_0, a_1, and a_2, we apply the following 3 conditions

$$u_p(x,0) = 0, \qquad \left.\frac{\partial u_p}{\partial y}\right|_{y=0} = \gamma(x), \qquad \int_0^h u_p(x,y)\,dy = 0. \qquad (26)$$

These set the desired gradient $\gamma(x)$ at the membrane surface while constraining u_p to have a zero mean. These require $a_0 = -h/16$, $a_1 = 3/(2h)$, and $a_2 = -5/h^3$. Solving for v_p from the continuity equation, we find that

$$v_p = -\frac{d\gamma}{dx}\left(a_0 \hat{y} + \frac{a_1 \hat{y}^3}{3} + \frac{a_2 \hat{y}^5}{5}\right). \qquad (27)$$

Note that the zero-mean condition on u_p forces $v_p = 0$ at $y = 0$ and h. As a final approximation, we approximate the CFD result for $\gamma(x)$ as

$$\gamma(x) = G\gamma^0\left[\beta + \cos\left(\frac{2\pi x}{\lambda}\right)\right], \qquad \gamma^0 = \left.\frac{\partial u_b}{\partial y}\right|_{x=y=0} = \frac{6U_{in}}{h}. \qquad (28)$$

The coefficient G sets the wave amplitude relative to γ^0, which is the base-state gradient $\partial u_b/\partial y$ at $(x, y) = (0, 0)$. The coefficient β forces $\gamma(x)$ to oscillate between $(\beta - 1)G\gamma^0 \leq \gamma(x) \leq (\beta + 1)G\gamma^0$. The downstream perturbation u_p is always positive near the membrane when $\beta > 1$. For $\beta < 1$, u_p can decelerate flow near the membrane, potentially introducing vortices. Fig. 13(b) shows that $G = 2.3$ and $\beta = 1.0$ reproduce CFD results for γ qualitatively well. Fig. 13(c) and (d) show
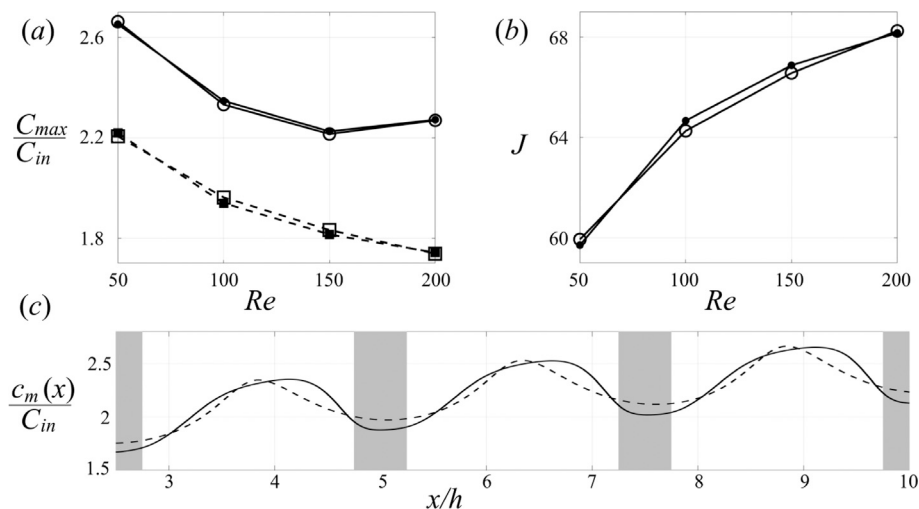
Fig. 14. Model and CFD results for the centerline arrangement using the tailored perturbation. (*a*) Comparison of CFD results for C_{max} (solid dots) and C_{osm} (solid squares) with model predictions for C_{max} (open circles) and C_{osm} (open squares). (*b*) Comparison of CFD (solid dots) and model (open circle) predictions for J. (*c*) Membrane concentration $c_m(x)$ predicted by CFD (solid line) and the tailored model (dashed line) when $Re = 50$.
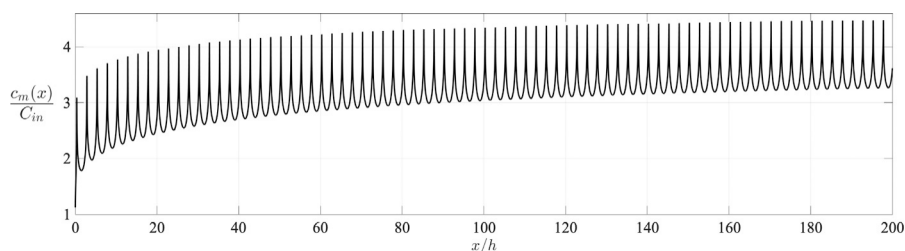

Fig. 15. Model predictions for $c_m(x)$ in an RO system of length $L = 40$ cm with the near-membrane arrangement. See text for details.

the velocity profiles extracted from the CFD and model at $x/h = 7$ for u^* and v, respectively. The model reproduces the CFD results qualitatively well.

We explored a range of G and β for $50 \leq Re \leq 200$ and calculated the best fit by minimizing the error, E, as in Section 5.1. Fig. 14(*a*–*b*) compares the resulting model and CFD predictions for C_{max}, C_{osm}, and J. The tailored model shows excellent agreement with the CFD results, producing relative errors on the order of 1% or less, compared to the 8% using the perturbation field derived in Eqs. (15)–(19). Fig. 14(*c*) compares the membrane concentration $c_m(x)$ for the model and CFD when $Re = 50$. The model reproduces the CFD result remarkably well.

5.3. Demonstration for long system lengths

As a final demonstration, we use our model to simulate the near-membrane arrangement in a feed channel of length $L = 40$ cm and height $h = 2$ mm (a length-to-height ratio of 200). We set $Re = 50$, and use the best-fit parameters $b = 1.7$ and $A = 0.75$ provided in Table B.1. The resulting salt concentration $c_m(x)$ along the membrane is shown in Fig. 15. We solve the advection equation using standard finite-volume methods detailed in [17]. Following a mesh-independence analysis, we use a grid with 20,000 cells in the x-direction and 128 cells in the y-direction (a total of 2,560,000 cells). The grid is uniform in the x-direction, but concentrated near the membrane using a Gauss–Lobatto–Chebyshev distribution, as detailed in Ref. [17]. The code is implemented in Matlab and run on a single core of a 2020 MacBook Pro with a 2 GHz Quad-Core Intel Core i5 processor. The total compute time is roughly one hour. In contrast, simulating a length-to-height ratio of 200 with CFD would require parallelized codes running on many cores of a supercomputer [19].

6. Conclusions

Our CFD simulations showed that spacer filaments generate regions of local solute accumulation in which the maximum concentration, C_{max}, can exceed twice the average value C_{osm}. Our experiments further confirmed that mineral scaling initiates in these regions. CFD also showed that while C_{osm} tends to decrease with increasing Reynolds number, C_{max} shows more complex non-monotonic variation, at times increasing with Reynolds number. Overall, we conclude that C_{osm} does not accurately predict the risk of mineral scaling.

For the operating conditions considered, the regions of solute accumulation were generated by vortical flow structures that appear on the membrane with a downstream wavelength set by the spacer geometry. We consequently sought a reduced model as the sum of a "base flow" ($\mathbf{v}_b$) and "perturbation flow" ($\mathbf{v}_p$). The base flow models a plate-and-frame RO system without spacers. The perturbation models spacers by superimposing an array of counter-rotating vortices near the membrane. We showed that the proper set of constraints simplifies the coupling of the flow fields at the membrane, and allows the concentration field to be solved using a simple fixed-point iteration.

To model different spacer arrangements, we proposed a family of perturbation fields defined by three parameters (λ, A, b) in Eqs. (15)–(19). By minimizing the weighted error proposed in Eq. (21), the reduced model reproduced CFD results for C_{max}, C_{osm}, and J very well for all three spacer arrangements. Moreover, the model also reproduced the spatial distribution $c_m(x)$ of solute on the membrane surface surprisingly well. The best agreement was observed for the near-membrane arrangement, for which the model reproduced CFD to within 3% relative error. The worst-case error for the remaining arrangements was only 8%, which occurred at $Re = 50$ for the centerline arrangement. Appendix B provides the fitting parameters A and b for the three spacer

arrangements for $50 \leq Re \leq 500$. Our intent is that one could improve agreement even further by leveraging CFD to develop perturbation fields ($\mathbf{v}_p$) tailored to specific spacer geometries. We demonstrated that approach by developing a field tailored to the centerline arrangement. The tailored field reproduced CFD data to within 1% relative error.

Here we emphasize that the reduced model provided a roughly 10,000-fold speed-up compared to CFD, and allowed us to simulate a feed channel with a length-to-height ratio of 200 using a simple Matlab code running on a single CPU core. Ongoing work is now expanding our model to 3D. For that purpose, one obvious approach is to obtain a 3D perturbation velocity field $\mathbf{v}_p$ directly from CFD. The CFD required for that purpose would be computationally cheap. If we leverage the assumption that $\mathbf{v}_p$ is periodic, and satisfies the no-slip and no-penetration conditions on the membrane, the perturbation field could be obtained by simulating a single unit cell of a periodic spacer geometry between two impermeable plates (ignoring the membrane). Periodic boundary conditions could also be applied in both the spanwise and downstream directions, making the simulation particularly easy to perform.

CRediT authorship contribution statement

Jacob Johnston: Conceptualization, Methodology, Software, Validation, Formal analysis, Investigation, Writing. **Sarah M. Dischinger:** Conceptualization, Methodology, Validation, Formal analysis, Investigation, Data curation, Writing – review & editing. **Mostafa Nassr:** Conceptualization, Methodology, Validation, Formal analysis, Investigation, Data curation, Writing – review & editing. **Ji Yeon Lee:** Conceptualization, Methodology, Validation, Formal analysis, Investigation, Data curation, Writing – review & editing. **Pedram Bigdelou:** Conceptualization, Methodology, Software, Validation, Formal analysis, Investigation. **Benny D. Freeman:** Conceptualization, Methodology, Supervision, Writing – review & editing. **Kristofer L. Gleason:** Conceptualization, Methodology, Supervision, Writing – review & editing. **Denis Martinand:** Conceptualization, Methodology, Writing – review & editing. **Daniel J. Miller:** Conceptualization, Methodology, Supervision, Writing – review & editing, Project administration, Funding acquisition. **Sergi Molins:** Conceptualization, Methodology, Formal analysis, Writing – review & editing. **Nicolas Spycher:** Conceptualization, Methodology, Formal analysis, Writing – review & editing. **William T. Stringfellow:** Conceptualization, Methodology, Formal analysis, Supervision, Writing – review & editing. **Nils Tilton:** Conceptualization, Methodology, Software, Validation, Formal analysis, Investigation, Resources, Writing, Supervision.

Declaration of competing interest

The authors declare that they have no known competing financial interests or personal relationships that could have appeared to influence the work reported in this paper.

Data availability

Data will be made available on request.

Acknowledgments

Table B.1
Reduced model fit for the near-membrane spacer arrangement.

Re	A	b	J (LMH)		C_{max}/C_{in}	
			CFD	ROM	CFD	ROM
50	0.750	1.7	59.99	59.98	3.589	3.589
100	0.836	1.5	65.34	64.18	3.312	3.253
150	0.800	1.5	67.15	65.76	3.212	3.138
200	0.773	1.5	67.88	66.37	3.134	3.064
250	0.752	1.5	67.99	66.45	3.146	3.074
300	0.739	1.5	68.07	66.57	3.135	3.067
350	0.731	1.5	67.76	66.63	3.112	3.162
400	0.728	1.5	67.44	67.10	3.041	3.028
450	0.728	1.5	69.12	67.83	3.008	2.950
500	0.728	1.5	70.11	68.45	2.952	2.882

Table B.2
Reduced model fit for the staggered spacer arrangement.

Re	A	b	J (LMH)		C_{max}/C_{in}	
			CFD	ROM	CFD	ROM
50	0.964	1.3	59.36	55.82	4.184	3.934
100	0.881	1.5	67.45	65.51	3.254	3.161
150	0.824	1.5	69.95	66.68	3.186	3.037
200	0.786	1.5	71.09	67.08	3.199	3.019
250	0.757	1.5	71.65	66.83	3.256	3.038
300	0.737	1.5	71.28	66.33	3.325	3.094
350	0.479	2.0	71.59	67.81	2.990	2.833
400	0.956	1.5	73.40	73.23	2.254	2.249
450	0.229	4.0	74.21	74.35	2.114	2.118
500	0.250	4.0	74.73	74.76	1.981	1.982

Appendix A. Thermophysical properties

We set the dynamic viscosity $\mu(c)$, density $\rho(c)$, and mass diffusivity $\mathcal{D}(c)$ of the aqueous NaCl solution using the relationships,

$$\mu(c) = A_v c^4 + B_v c^3 + C_v c^2 + D_v c + E_v. \tag{29}$$

$$A_v = -1.63 \times 10^{-14}, \quad B_v = 1.57 \times 10^{-11}, \quad C_v = 1.04 \times 10^{-9}, \tag{30}$$

$$D_v = 1.35 \times 10^{-6}, \quad E_v = 8.90 \times 10^{-4}. \tag{31}$$

$$\rho(c) = A_\rho c^3 + B_\rho c^2 + C_\rho c + D_\rho. \tag{32}$$

$$A_\rho = 1.56 \times 10^{-7}, \quad B_\rho = -1.92 \times 10^{-4}, \quad C_\rho = 0.68, \quad D_\rho = 997.$$

$$\mathcal{D}(c) = 10^{-09} \times \frac{A_d + \frac{1000}{\mathcal{M}} B_d c}{1 + \frac{1000}{\mathcal{M}} C_d c + D_d (\frac{1000 c}{\mathcal{M}})^2}. \tag{33}$$

$A_d = 1.418, \quad B_d = 1.159 \times 10^{-01}, \quad C_d = 8.50 \times 10^{-02}, \quad D_d = 1.514 \times 10^{-05}$, where concentration is measured in g/l and Eq. (33) is valid for $c < 7.71$ g/l of NaCl. Here $\mathcal{M} = 58.44$ g/mol is the molecular weight of NaCl. These relationships assume $T_{in} = 25$ °C. The correlations for $\mu(c)$ and $\rho(c)$ were derived using the OLI Stream Analyzer database (OLI Systems, Morris Plains, NJ). We obtained the correlation for $\mathcal{D}(c)$ from Ref. [21].

Appendix B. Fitting data

In this section, we provide the fitting data for the results shown in Section 5.1 and for the tailored perturbation field developed in Section 5.2 (see Tables B.2–B.4).

Appendix C. Supplementary data

Supplementary material related to this article can be found online at https://doi.org/10.1016/j.memsci.2023.121508.

Table B.3
Reduced model fit for the centerline spacer arrangement.

Re	A	b	J (LMH)		C_{max}/C_{in}	
			CFD	ROM	CFD	ROM
50	0.044	30	59.71	59.94	2.653	2.876
100	0.028	30	64.66	64.26	2.347	2.468
150	0.020	40	64.66	65.52	2.226	2.325
200	0.014	40	68.16	68.24	2.272	2.331
250	0.030	14	69.44	69.42	2.478	2.478
300	0.249	4.0	73.12	73.02	2.201	2.198
350	0.049	14	74.38	74.24	1.950	1.947
400	0.018	40	74.76	74.92	1.795	1.796
450	0.352	4.0	75.91	75.47	1.887	1.877
500	0.777	2.0	75.70	74.90	2.008	1.987

Table B.4
Reduced model fit for the tailored perturbation for the centerline arrangement.

Re	G	β	J (LMH)		C_{max}/C_{in}	
			CFD	ROM	CFD	ROM
50	2.432	1.0	59.71	59.94	2.653	2.663
100	2.284	1.0	64.66	64.26	2.347	2.333
150	2.657	0.9	66.87	66.56	2.226	2.215
200	3.688	0.8	68.16	68.24	2.272	2.270

References

[1] A. Efraty, J. Septon, Closed circuit desalination series no-5: high recovery, reduced fouling and low energy nitrate decontamination by a cost-effective BWRO-CCD method, Desalin. Water Treat. 49 (1–3) (2012) 384–389.

[2] R.L. Stover, Permeate recovery and flux maximization in semibatch reverse osmosis, IDA J. Desalination Water Reuse 5 (1) (2013) 10–14.

[3] B. Mansell, P. Ackman, C. Tang, P. Friess, Pilot-scale evaluation of the closed-circuit desalination process for minimizing RO concentrate disposal volume, in: WateReuse California Annual Conference, Los Angeles, CA, March 15-17, 2015.

[4] R. Stover, E. Idica, High reliability and maximum recovery water reuse with closed circuit reverse osmosis, in: Proceedings of the International Desalination Association Conference on Water Reuse, Nice, France, 2016.

[5] X. Chen, N.Y. Yip, Unlocking high-salinity desalination with cascading osmotically mediated reverse osmosis: Energy and operating pressure analysis, Enviromen. Sci. Technol. Lett. 52 (2018) 2242–2250.

[6] Z. Wang, A. Deshmukh, Y. Du, M. Elimelech, Minimal and zero liquid discharge with reverse osmosis using low-salt-rejection membranes, Water Res. 170 (2020) 115317.

[7] D.M. Davenport, A. Deshmukh, J.R. Werber, M. Elimelech, High-pressure reverse osmosis for energy-efficient hypersaline brine desalination: Current status, design considerations, and research needs, Enviromen. Technol. Lett. 5 (2018) 467–475.

[8] J. Borden, J. Gilron, D. Hasson, Analysis of RO flux decline due to membrane surface blockage, Desalination 66 (1987) 257–269.

[9] M. Brusilovsky, J. Borden, D. Hasson, Flux decline due to gypsum precipitation on ro membranes, Desalination 86 (1992) 187–222.

[10] M. Uchymiak, E. Lyster, J. Glater, Y. Cohen, Kinetics of gypsum crystal growth on a reverse osmosis membrane, J. Membr. Sci. 314 (2008) 163–172.

[11] A.I. Radu, M.S.H. van Steen, J.S. Vrouwenvelder, M.C.M. van Loosdrecht, C. Picioreanu, Spacer geometry and particle deposition in spiral wound membrane feed channels, Water Res. 64 (2014) 160–176.

[12] A.I. Radu, L. Bergwerff, M.C.M. van Loosdrecht, C. Picioreanu, A two-dimensional mechanistic model for scaling in spiral wound membrane systems, Chem. Eng. J. 214 (2014) 77–91.

[13] H.-J. Oh, Y.-K. Choung, S. Lee, J.-S. Choi, T.-M. Hwang, J.H. Kim, Scale formation in reverse osmosis desalination: model development, Desalination 238 (2009) 333–346.

[14] E. Lyster, J. Au, R. Rallo, F. Giralt, Y. Cohen, Coupled 3-D hydrodynamics and mass transfer analysis of mineral scaling-induced flux decline in a laboratory plate-and-frame reverse osmosis membrane module, J. Membr. Sci. 339 (1) (2009) 39–48, http://dx.doi.org/10.1016/j.memsci.2009.04.024, URL https://www.sciencedirect.com/science/article/pii/S1383586617324188.

[15] A. Haidari, S. Heijman, W. van der Meer, Optimal design of spacers in reverse osmosis, Sep. Purif. Technol. 192 (2018) 441–456, http://dx.doi.org/10.1016/j.seppur.2017.10.042, URL https://www.sciencedirect.com/science/article/pii/S1383586617324188.

[16] T. Xu, E. Sonnenthal, N. Spycher, K. Pruess, Toughreact—a simulation program for non-isothermal multiphase reactive geochemical transport in variably saturated geologic media: Applications to geothermal injectivity and CO$_2$ geological sequestration, Comput. Geosci. 32 (2) (2006) 145–165, http://dx.doi.org/10.1016/j.cageo.2005.06.014, URL https://www.sciencedirect.com/science/article/pii/S0098300405001500.

[17] J. Johnston, J. Lou, N. Tilton, Application of projection methods to simulating mass transport in reverse osmosis systems, Comput. & Fluids 232 (2022) http://dx.doi.org/10.1016/j.compfluid.2021.105189.

[18] J. Lou, J. Johnston, T.Y. Cath, D. Martinand, N. Tilton, Computational fluid dynamics simulations of unsteady mixing in spacer-filled direct contact membrane distillation channels, J. Membr. Sci. 622 (2021) 118931, http://dx.doi.org/10.1016/j.memsci.2020.118931, URL https://www.sciencedirect.com/science/article/pii/S0376738820315052.

[19] H. Sitaraman, I. Battiato, Impact of large-scale effects on mass transfer and concentration polarization in reverse osmosis membrane systems, Sep. Purif. Technol. 303 (2022) 122121, http://dx.doi.org/10.1016/j.seppur.2022.122121, URL https://www.sciencedirect.com/science/article/pii/S1383586622016768.

[20] S.S. Bucs, A.I. Radu, V. Lavric, J.S. Vrouwenvelder, C. Picioreanu, Effect of different commercial feed spacers on biofouling of reverse osmosis membrane systems: A numerical study, Desalination 343 (2014) 26–37.

[21] E. Lyster, Y. Cohen, Numerical study of concentration polarization in a rectangular reverse osmosis membrane channel: permeate flux variation and hydrodynamic end effects, J. Membr. Sci. 303 (1) (2007) 140–153, http://dx.doi.org/10.1016/j.memsci.2007.07.003, URL https://www.sciencedirect.com/science/article/pii/S0376738807004711.

[22] V. Gekas, B. Hallström, Mass transfer in the membrane concentration polarization layer under turbulent cross flow I. Critical literature review and adaption of existing sherwood correlations to membrane operations, J. Membr. Sci. 30 (1987) 153–170.

[23] V. Geraldes, V. Semião, M.N. de Pinho, The effect of the ladder-type spacers configuration in nf spiral-wound modules on the concentration boundary layers disruption, Desalination 146 (1) (2002) 187–194, http://dx.doi.org/10.1016/S0011-9164(02)00467-8, URL https://www.sciencedirect.com/science/article/pii/S0011916402004678.

[24] V. Geraldes, V. Semião, M.N. de Pinho, Flow management in nanofiltration spiral wound modules with ladder-type spacers, J. Membr. Sci. 203 (1) (2002) 87–102, http://dx.doi.org/10.1016/S0376-7388(01)00753-0, URL https://www.sciencedirect.com/science/article/pii/S0376738801007530.

[25] C.H.K. Williamson, Vortex dynamics in the cylinder wake, Annu. Rev. Fluid Mech. 28 (1) (1996) 477–539, http://dx.doi.org/10.1146/annurev.fl.28.010196.002401.

[26] L. Zovatto, G. Pedrizzetti, Flow about a circular cylinder between parallel walls, J. Fluid Mech. 440 (2001) 1–25, http://dx.doi.org/10.1017/S0022112001004608.

[27] M. Sahin, R.G. Owens, A numerical investigation of wall effects up to high blockage ratios on two-dimensional flow past a confined circular cylinder, Phys. Fluids 16 (5) (2004) 1305–1320.

[28] E.M.V. Wagner, A.C. Sagle, M.M. Sharma, B.D. Freeman, Effect of crossflow testing conditions, including pH and continuous feed filtration, on commercial reverse osmosis membrane performance, J. Membr. Sci. 345 (2009).

[29] C.E. Harvie, N. Møller, J.H. Weare, The prediction of mineral solubilities in natural waters: The Na-K-Mg-Ca-H-Cl-SO$_4$-OH-HCO$_3$-CO$_3$-CO$_2$-H$_2$O system to high ionic strengths at 25° c, Geochim. Cosmochim. Acta 48 (4) (1984) 723–751, http://dx.doi.org/10.1016/0016-7037(84)90098-X, URL https://www.sciencedirect.com/science/article/pii/001670378490098X.

[30] J.G. Wijmans, R. Baker, The solution-diffusion model: a review, J. Membr. Sci. 107 (1995).

[31] S.R. Charlton, D.L. Parkhurst, Modules based on the geochemical model phreeqc for use in scripting and programming languages, Comput. Geosci. 37 (2011) 1653–1663.

[32] A. Matin, F. Rahman, H.Z. Shafi, S.M. Zubair, Scaling of reverse osmosis membranes used in water desalination: Phenomena, impact, and control; future directions, Desalination 455 (2019) 135–157, http://dx.doi.org/10.1016/j.desal.2018.12.009, URL https://www.sciencedirect.com/science/article/pii/S0011916418318897.

[33] K. Johnson, The calculation of ion pair diffusion coefficients: A comment, Mar. Chem. 10 (1980) 195–208.

[34] W.-Y. Shih, A. Rahardianto, R.-W. Lee, Y. Cohen, Morphometric characterization of calcium sulfate dihydrate (gypsum) scale on reverse osmosis membranes, J. Membr. Sci. 252 (1) (2005) 253–263, http://dx.doi.org/10.1016/j.memsci.2004.12.023, URL https://www.sciencedirect.com/science/article/pii/S0376738804008336.

[35] I. OLI Systems, https://www.olisystems.com/ (2022).

[36] P. Haldenwang, Laminar flow in a two-dimensional plane channel with local pressure-dependent crossflow, J. Fluid Mech. 593 (2007) 463–473, http://dx.doi.org/10.1017/s0022112007008622.

[37] P. Haldenwang, P. Guichardon, G. Chiavassa, N. Ibaseta, Exact solution to mass transfer in Berman flow: Application to concentration polarization combined with osmosis in crossflow membrane filtration, Int. J. Heat Mass Transfer 53 (19–20) (2010) 3898–3904, http://dx.doi.org/10.1016/j.ijheatmasstransfer.2010.05.008.

[38] B. Bernales, P. Haldenwang, Laminar flow analysis in a pipe with locally pressure-dependent leakage through the wall, Eur. J. Mech. B/Fluids 43 (2014) 100–109, http://dx.doi.org/10.1016/j.euromechflu.2013.07.006.

[39] B. Bernales, P. Haldenwang, P. Guichardon, N. Ibaseta, Prandtl model for concentration polarization and osmotic counter-effects in a 2-D membrane channel, Desalination 404 (2017) 341–359, http://dx.doi.org/10.1016/j.desal.2016.09.026.

[40] N. Tilton, D. Martinand, E. Serre, R.M. Lueptow, Incorporating Darcy's law for pure solvent flow through porous tubes: Asymptotic solution and numerical simulations, AIChE J. 58 (7) (2012) 2030–2044, http://dx.doi.org/10.1002/aic.13823, arXiv:https://aiche.onlinelibrary.wiley.com/doi/pdf/10.1002/aic.13823, URL https://aiche.onlinelibrary.wiley.com/doi/abs/10.1002/aic.13823.

[41] S.A. Regirer, On the approximate theory of the flow of a viscous incompressible liquid in a tube with permeable walls, Soviet Physics, Tech. Phys. 5 (1960) 602–605.

[42] A.S. Berman, Laminar flows in channels with porous walls, J. Appl. Phys. 24 (1953) 1232–1235.